Topological electronic state and anisotropic Fermi surface in half-Heusler GdPtBi

Junli Zhang,[1] Jie Chen,[2] Peng Li,[1] Chenhui Zhang,[1] Zhipeng Hou,[2] Yan Wen,[1] Qiang Zhang,[1] Wenhong Wang,[2]* and Xixiang Zhang[1]*

[1]King Abdullah University of Science and Technology (KAUST), Division of Physical Science and Engineering (PSE), Thuwal 23955-6900, Saudi Arabia.

[2]State Key Laboratory for Magnetism, Beijing National Laboratory for Condensed Matter Physics, Institute of Physics, Chinese Academy of Sciences, Beijing 100190, China.

*Authors to whom correspondence should be addressed: wenhong.wang@iphy.ac.cn and xixiang.zhang@kaust.edu.sa.

Abstract

Half-Heusler alloys possess unique and desirable physical properties due to their thermoelectricity, magnetism, superconductivity, and weak antilocalization effects. These properties have become of particular interest since the recent discovery of topological Weyl semimetal state for which the electronic bands are dispersed linearly around one pair of Weyl nodes, with opposite chirality (i.e., chiral anomaly). Here, we report the transport signatures of topological electronic state in a half-Heusler GdPtBi single crystal. We show that the non-trivial π Berry phase, negative magnetoresistance and giant planner Hall effect arise from the chiral anomaly and that the Shubnikov-de Haas (SdH) oscillation frequency in GdPtBi is angle-dependent with an anisotropic Fermi surface (FS). All transport signatures not only demonstrate the topological electronic state in half-Heusler GdPtBi crystals, but also describe the shape of the anisotropy FS.

1. Introduction

Ternary half-Heusler compounds crystallize in a cubic MgAgAs type structure, which belongs to the space group $F\bar{4}3m$ and exhibits tunable electron properties as varying the components in the chemical formula XYZ (where X and Y are transition or rare earth metals and Z is the main-group element)[1-3]. Then, many fantastic properties of the compounds, including the thermoelectricity[4], unusual magnetism[5], superconductivity[6], weak anti-localization effect[7] are being widely explored due to the variable electronic states. This becomes more attractive since the discovery of topological Weyl semimetal states in half-Heusler compounds[8], in which the electronic band can be dispersed linearly around one pair of Weyl nodes with opposite chirality (i.e., chiral anomaly). The significance of Weyl/Dirac semimetal as a representative quantum material has been extensively studied for their potential applications and fascinating physics[9,10]. For example, in Dirac semi-metals, each Dirac cone is the result of the superposition of two Weyl nodes with opposite chirality. The Weyl nodes could be separated in the momentum space once the time-reversal or inversion symmetry, or both, are broken, making it impossible to generate a fully gapped insulating state[11]. In theory, the massless Weyl fermions can drive exotic topological phenomena and chiral anomaly related quantum transport properties, if they are located close enough to the Fermi level[12,13]. Thus, studying the chiral anomaly and recognizing the Fermi surface (FS) become ever more important not only for Weyl semimetals but also for half-Heusler compounds.

The topological Weyl semimetal state has two transport signatures, in which the relation of negative magnetoresistance (NMR) to the suppressed backscattering electrons with opposite chirality[14,15], as well as the origination of the giant planar Hall effect (PHE) from the chiral magnetic effect[16,17] are being theoretically studied and confirmed. However, the exact origin of

these transport phenomena and the shape of the FS remain unclear, especially in the Weyl semimetal GdPtBi. Herein, we perform magneto-transport experiments on a half-Heusler GdPtBi crystal, which is an essential member of half-Heusler compounds featuring a frustrated antiferromagnetic lattice and an inverted band structure[18]. We study the non-trivial π Berry phase, NMR and PHE and find that the amplitude of PHE can be divided into two field-regions, in agreement with theoretical predictions. Our temperature-dependent transport study allows us to conclude that the PHE in GdPtBi should originate from the chiral anomaly. In addition, the shape of Fermi pocket in GdPtBi sketched by the angle-dependent magnetoresistance (MR) measurements is shown to be anisotropic. Thus, our results not only demonstrate the topological electronic state of the half-Heusler GdPtBi, but also describes the shape of the FS.

2. Experimental detail and methods

Single GdPtBi crystals were synthesized by a Bi-flux method. First, we mixed high-purity raw materials of Gd (ingot, 99.99%), Pt (ingot, 99.99%) and Bi (ingot, 99.99%) at a molar ratio of 1:1:20 using an alumina crucible. Prior to mixing, the oxide layer on the Gd ingot surface was removed by grinding. Note that the Bi act as not only the reactant but also solvent (i.e., flux) during the GdPtBi crystals growth, that is why the excess Bi should be ensured in the precursors. The whole procedures were carried out in an argon-filled glove box, in which the content of O_2 and H_2O was strictly controlled below 0.5 ppm. The alumina crucible and raw materials were sealed inside a tantalum tube under a proper Ar pressure; the tantalum tube was then further sealed into an evacuated quartz tube. The crystal growth was carried out in a furnace by heating the tube from room temperature to 1150 °C, for 10 h, and kept at 1150 °C for 48 h, before being slowly cooled to 650 °C, at a rate of 2 °C/h. Lastly, the excess of Bi flux was removed by centrifuging the tube at 650 °C.

The crystal structure, orientation, crystalline quality and chemical composition of the GdPtBi single crystal was analyzed using an X-ray diffraction (XRD) instrument and transmission electron microscope (TEM, FEI Titan Cs probe). High-angle annular dark-field scanning transmission electron microscopy (HAADF-STEM) was carried out with an inner semi-angle of 80 mrad and a 250 mrad outer semi-angle. The TEM specimens were prepared using a FEI dual-beam focused ion beam-scanning electron microscope (FIB/SEM, FEI Helios G4 UX). STEM HAADF image simulations were performed with the Dr. Probe software package[19]. Models of the atomic structure were built based on a cubic unit cell ($F\bar{4}3m$ space group) with a lattice constant a = 6.682 Å. The high voltage, Cs coefficient, Cc coefficient, thickness and defocus were 300 kV, 50 μm, 0 mm, 40 nm and 0 nm, respectively. The supercells used in the calculations extended over 4 × 4 unit cells projected on the (100) plane.

The GdPtBi single crystal was polished to a thickness of 0.1 mm for the transverse MR measurement (as shown in **Figure S1**). The four-probe method was applied for measurement, and the electrical leads were attached to the sample by platinum wires, using silver paste. To minimize the misalignment of the device for the PHE measurement, the FIB/SEM technique was used to prepare the Hall bar device (in (111) plane) that was lifted out from a bulk GdPtBi single crystal. The width, length and thickness of the device for PHE were 5 μm, 10 μm, and 1.5 μm, respectively. The MR and PHE were measured using a Quantum Design physical properties measurement system (PPMS) equipped with a temperature range of 2 K-300 K.

3. Results and discussion

The polyhedral characteristic of as-prepared GdPtBi crystals with a size of 3.0 × 2.3 × 0.5 mm^3 is presented in **Figure 1**a. The molar ratio of Gd, Pt, and Bi was confirmed to be 32.3:33.3:34.1 by

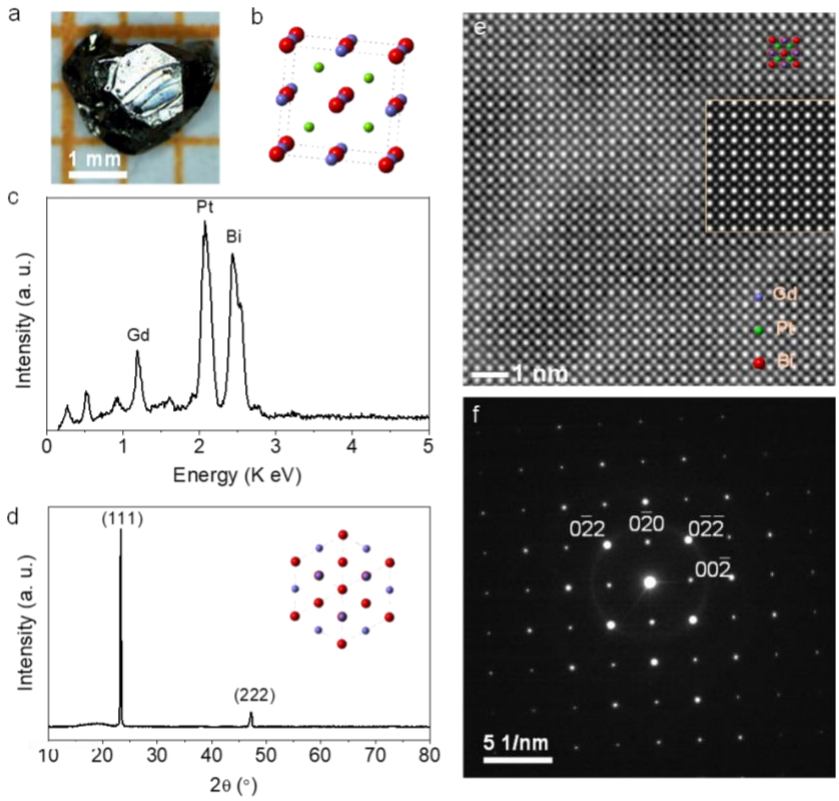

Figure 1. (a)-(d) Photograph, crystal structure, EDX and XRD pattern of as-prepared GdPtBi single crystal, respectively; (e) Experimental and theoretical high-resolution TEM images along the [100] zone axis of the GdPtBi; (f) Selected area electron diffraction (SAED) patterns.

the energy-dispersive X-ray (EDX), demonstrating the accuracy of the chemical component and formula in GdPtBi (Figure 1c). Specifically, we found that the GdPtBi was the single crystal that crystallized in a cubic MgAgAs type structure along the [111] direction, as confirmed by the (*l l l*) reflection in the XRD pattern (Figure 1d). The crystal structure of the single-crystal was further studied by the HAADF-STEM image and selected area electron diffraction (SAED) pattern. These results demonstrate that there are no bismuth impurities, stacking faults, and/or amorphous regions in the GdPtBi crystal (Figure 1c-d). The atomic columns contrast between the ideal cubic GdPtBi (the inset of Figure 1e) and the experimental STEM image were also found to be consistent, fully

demonstrating the good crystal quality of GdPtBi. All characterizations confirmed the single-crystal features of our GdPtBi in a cubic MgAgAs-type structure of high quality.

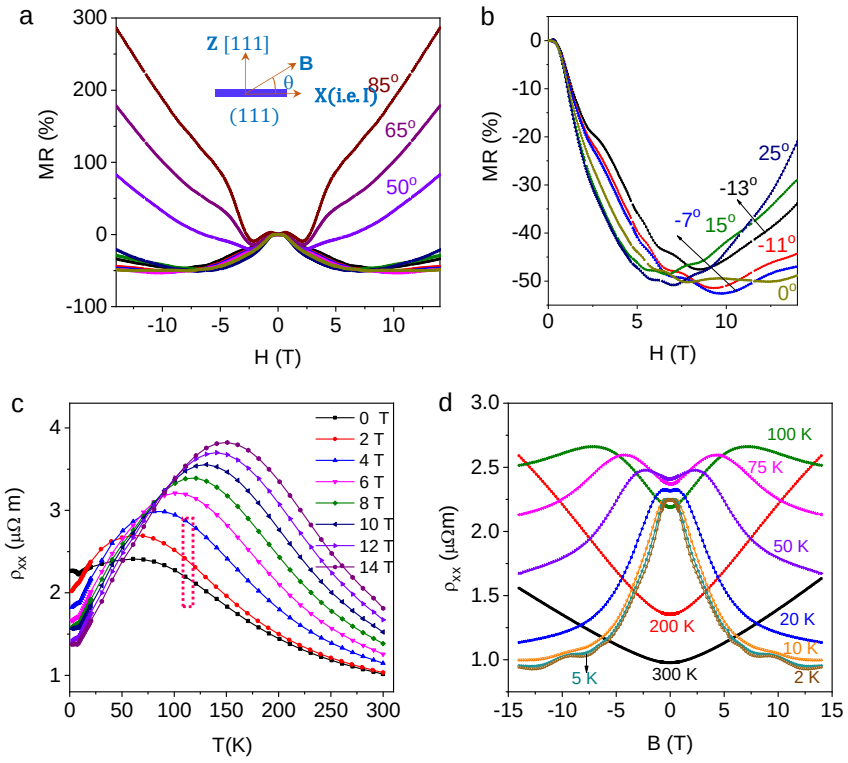

Figure 2. (a) Variation of MR versus B at 2 K, measured at various out-of-plane angles θ; (b) Magnified view of NMR; (c) Temperature dependence of longitudinal resistivity ρ_{xx} for temperatures ranging from 2 K-300 K, under different external magnetic fields; (d) Longitudinal magnetoresistivity (LMR) $\rho_{xx}(B)$ for temperatures ranging from 2 K-300 K with B// I//x; LMR with a bell-shaped profile is observed in $\rho_{xx}(B)$ up to 100 K.

The FS topology (i.e., chiral anomaly) of GdPtBi was investigated first by the means of MR, with the current applied parallel to the surface of the single crystal (i.e., (111) plane). The angle-dependent longitudinal resistivity (ρ_{xx}) measured at 2 K is presented in **Figure 2**a, in which the θ is defined as the angle between current (I) and the applied magnetic field (B) (inset of Figure 2a). We find that the MR increases linearly up to 285% at 14 T, when the tilted angle $\theta = 85°$; on the

other hand, the MR decreases as the tilted angle θ decreases from 85° to 25°). Moreover, the NMR appeared in the low-field region where θ is lower than 25° (i.e., $\theta < 25°$). This phenomenon becomes the most prominent when θ decreases to 0° (magnified view in Figure 2b).

Deeper physical insights can be gained through the transport properties of the device in the presence of collinear external electric and magnetic fields (θ = 0°). Figure 2c shows the temperature dependence ρ_{xx} at the selected field, which is consistent with the previous results[8]. Besides, the antiferromagnetic ordering in GdPtBi at about 9.7 K (i.e., inflection points in ρ_{xx} curves) was also observed, which should originate from the frustrated *fcc* lattice caused by Gd atoms[18]. The temperature of the phase transition is consistent with the hysteresis loops (Figure S2). We also find that the NMR can be suppressed as the temperature increases (i.e., a prominent NMR at the low temperature), and can ultimately disappear at 200 K, as confirmed by the LMR for a temperature range of 2-300 K (Figure 2d). These behaviors are similar to those observed in Dirac/Weyl semi-metals (e.g., Cd_3As_2, WTe_2, TaAs)[12,20,21], demonstrating the existence of chiral anomaly associated fermions in GdPtBi.

In addition, the topological electronic state in GdPtBi was further confirmed by the origination of the NMR. Generally, the chiral anomaly[21], current jetting effect[21], or magnetism[22] can give rise to the NMR. We firstly exclude the possibilities originating from the current jetting effect (relate to the geometry or size effects of samples). This is because there are no characteristic dips, hump or negative voltage of the current jetting effect that can be observed in the angular dependence ρ_{xx} (**Figure S3**). Besides, the Néel temperature of the pronounced antiferromagnetic ordering (~9.7 K) is much lower than 100 K for the appearance of the NMR, which also excludes the origination from the antiferromagnetism of GdPtBi. Thus, we conclude that the NMR arises

from the suppressed backscattering electrons with opposite chirality (i.e., Weyl fermions) in GdPtBi.

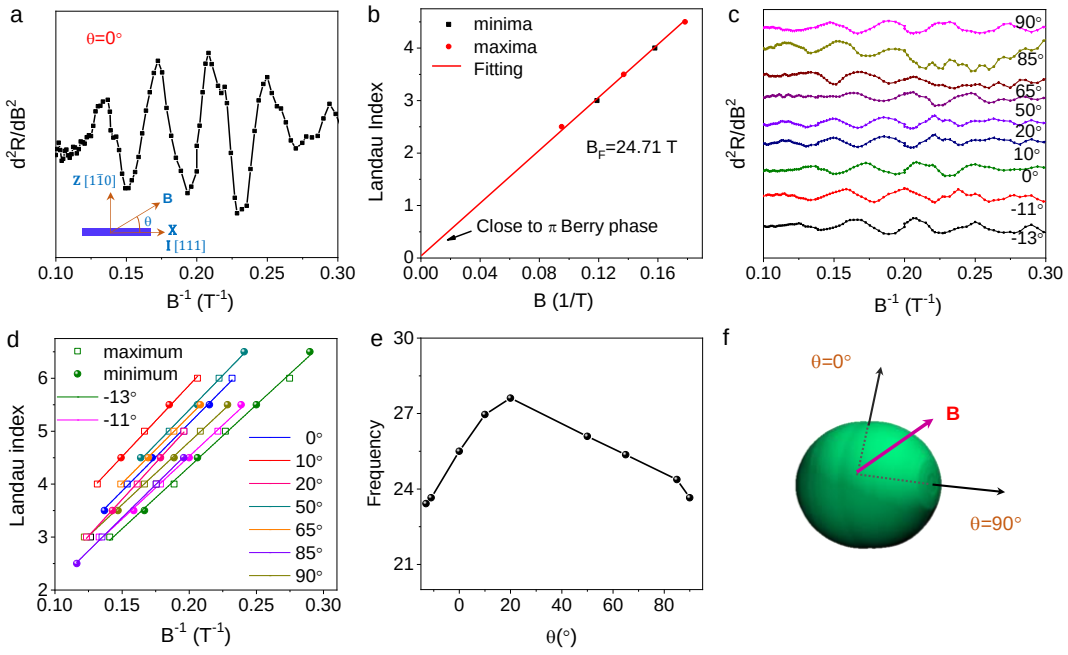

Figure 3. (a)-(b) Shubnikov de Haas (SdH) oscillations and Landau index *n* as a function of 1/B at θ = -0°, respectively; (c)-(d) SdH oscillations and Landau index *n* versus 1/*B* between θ = -13° to 90°; (e) Angle-dependent frequency of the SdH oscillation indicating an anisotropy of the FS in GdPtBi; (f) Sketched Fermi pocket of GdPtBi.

The pronounced Shubnikov-de Hass (SdH) oscillations can be also observed in the LMR curves (Figure 2b, 2d) at low temperatures, by which the inherent quantum mechanical nature of GdPtBi can be further analyzed. We calculated $d^2\rho/dB^2$ to reveal these SdH oscillations and explore the physics of the quantum transport underlying the experimental data. We found that the SdH oscillations were more obvious in the curves of $d^2\rho/dB^2$ *vs* B^{-1} at 2 K (**Figure 3**a). Then, the Berry phase and the shape of the FS can be extracted and reconstructed, respectively. In more detail, the Landau fan diagram was plotted according to the Lifshitz-Onsager quantization rule[23],

$F/B = n - \gamma + \delta$, wherein F and n are the oscillation frequency and Landau index, respectively (Figure 3b). The Onsager phase $\gamma = 1/2 - \phi_B/2\pi$ and the additional phase shift factor δ changed from 0 to ±1/8, depending on the curvature of the FS in the third direction. Figure 3d presents a detailed Landau fan at $\theta = 0°$, which gives an intercept of about 0.06 and corresponds to a 0.88 π Berry phase. These values demonstrate the nontrivial Berry phase feature when $B//I$. Note that the SdH oscillation frequency of this GdPtBi crystal is about 24.71 T (Figure 3b). Then, we studied the angular-dependent of SdH oscillations at 2 K to gain more insight into the topology of the FS in GdPtBi (Figure 3c). A Periodic oscillation can be observed in all directions, but with slightly different periods, indicating the anisotropic nature of the FS of GdPtBi, at high field. Besides, we find that the cross-sectional areal of the FS reaches a maximal value at $\theta = 20°$, and then decreases to a minimum value at $\theta = 90°$ (Figure 2e). This angle-dependent behavior of the FS is similar to that of half-Heusler LuPtBi[24]. Thus, the shape of the FS of Weyl semi-metal GdPtBi can be sketched, based on the angular-dependent oscillation frequency (Figure 3f).

Another phenomenon related to the topological electronic state is the PHE**,** where the current, Hall voltage and magnetic field are coplanar. The angular dependence of PHE in Weyl semimetals can be formulated as[16]:

$$\rho_{xy}^{planar} = -\Delta\rho^{chiral} sin\varphi cos\varphi \quad (1)$$

where φ is the angle between the magnetic field and the current, $\Delta\rho^{chiral} = \rho_{\perp} - \rho_{//}$ is the resistivity anisotropy induced by the chiral anomaly, $\rho_{\perp}$ and $\rho_{//}$ are the resistivities for the magnetic field in both perpendicular and parallel directions to the current, respectively. Herein, a typical GdPtBi device and measurement configuration of PHE are represented in **Figure 4**a, in which the current I is applied along the longitudinal direction of the devices. The angle-dependent planar Hall resistivity ρ_{xy} are recorded at different fields and temperatures when the sample is

rotated in the fields-plane from 0° to 360°. The angular dependence of $\rho_{xy}(B)$ under magnetic fields of 9 T and -9 T at 2 K is presented in Figure 4b. We find that the shape of ρ_{xy} (B) curves is asymmetric and angular-dependent, which can be attributed to the normal Hall effect arising from the perpendicular component of the magnetic field. Several steps need to be taken, as shown below, to get the intrinsic PHE.

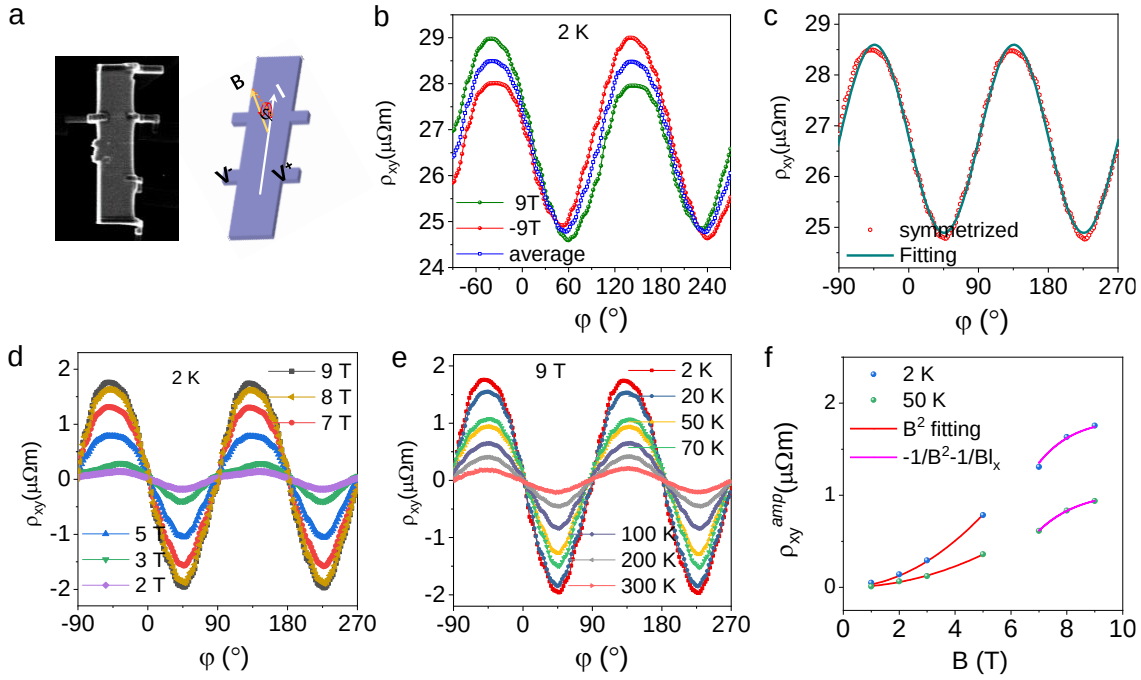

Figure 4. (a) SEM image of the GdPtBi device and schematic illustration of the measurement configuration; (b) Planar transverse magnetoresistivity ρ_{xy} measured at 2 K under $B = \pm 9$ T; (c) Symmetrized planar transverse magnetoresistivity ρ_{xysym} and fitting curve at 2K and $|B| = 9$ T; (d) Intrinsic PHE ($\rho_{xyplanar}$) versus φ under various magnetic fields at 2 K; (e) Angular dependence of $\rho_{xyplanar}$ at various temperatures ($B = 9$ T); (f) Field dependence of the amplitude of $\rho_{xyplanar}$ at 2 K and 50 K.

The first, the normal Hall resistivity can be removed by symmetrizing the $\rho_{xy}(B)$ curves *via* $\rho_{xy}^{sym} = 0.5\times[\rho_{xy}(B) + \rho_{xy}(-B)]$ when the perpendicular component is introduced by the

misalignment between the device plane and the magnetic field (i.e., the green and red curves in Figure 4b). We find that the $\rho_{xy}{}^{sym}$ becomes more symmetric (the blue curve in Figure 4b), but the data still cannot be described by Eq. 1 due to an obvious resistivity shift away from zero. This shift should originate from the misalignment of the Hall bar, which can generate a planar LMR component coupled to the $\rho_{xyplanar}$. Thus, we describe the ρ_{xysym} by the modified equation (2), after considering this misalignment[17]:

$$\rho_{xy}{}^{sym} = -\Delta\rho^{chiral} sin\varphi cos\varphi + a\Delta\rho^{chiral} cos^2\varphi + b \quad (2)$$

The three terms in Eq. 2 correspond to the intrinsic PHE caused by the chiral anomaly and the in-plane anisotropic MR and LMR offset originating from the geometric misalignment of the Hall device, respectively. The symmetrized $\rho_{xy}{}^{sym}$ can be fitted well using Eq. 2, as demonstrated by the blue curve in Figure 4c. Hence, the intrinsic PHE can be obtained after subtracting the normal Hall resistivity and planar LMR component (Figure 4d, 4e). We find that the $\rho_{xyplanar}$ can be increased monotonically when increasing the field, and that the $\rho_{xyplanar}$ can be decreased as increasing the temperature under various magnetic fields at 2 K (Figure 4d, 4e). It should be noted that the $\rho_{xyplanar}$ decreases monotonically with increasing temperature (Figure 4e). This is attributed to the fact that the Weyl points of GdPtBi can move farther away from the Fermi level when the temperature increases (Figure 4e). Thus, these phenomena are consistent with those observed for other Weyl semi-metals previously reported[25].

More physical insights of the PHE in GdPtBi can be obtained from the extracted amplitudes of PHE ($\rho_{xy}{}^{amp}$), which are directly related to the anisotropic resistivity originating from the chiral anomaly. The $\rho_{xy}{}^{amp}$ versus *B* extracted from the $\rho_{xy}{}^{sym}$ at 2 K (Figure 4d) and 50 K (Figure S4) are shown in Figure 4f. We find that the results cannot follow the simple quadratic magnetic field dependence, which is different for traditional magnetic materials[26]. This is because the theoretical

prediction of the magnitude of PHE in a Weyl/Dirac semi-metal can be divided into two field-dependent regions: the weak magnetic- field regime and the sample size related to the stronger-field regime. In the weak magnetic field region, $l_a \gg l_c$, the PHE is given by[16],

$$\rho_{xy}{}^{amp} \propto \left(\frac{l_c}{l_a}\right)^2 \propto B^2 \quad (3)$$

For the more complicated, stronger field- region, where $l_a \ll l_c$ and $l_x > l_a$, the PHE has the following form:

$$\rho_{xy}{}^{amp} \propto -\left(\frac{l_a}{l_c}\right)^2 - \frac{l_a}{l_x} \propto -\frac{1}{B^2} - \frac{1}{Bl_x} \quad (4)$$

where $l_a = \frac{D}{\Gamma B}$, $l_c = \sqrt{D\tau_c}$ and l_x are the chiral anomaly related magnetic length, chiral charge diffusion length and Hall bar length, respectively. The parameters of D, B, Γ and τ_c are the diffusion coefficient, magnetic field, transport coefficient and chiral charge relaxation time, respectively. We find that the ρ_{xyamp} are fit well with a B^2 and $-\frac{1}{B^2} - \frac{1}{Bl_x}$ function in the low field regime ($B \leq 5$ T) and high field regime ($B \geq 6$ T), respectively. The consistency between the experimental observations and the theory further demonstrates the existence of chiral anomaly in GdPtBi.

4. Conclusion

In summary, we have observed the transport signatures of a non-trivial π Berry phase, NMR and the giant PHE in a half-Heusler GdPtBi single-crystal, in which the NMR and PHE were confirmed to be induced both by the chiral anomaly. We find that the SdH oscillation frequency is angle-dependent, and it show that the Fermi-surface is anisotropic in GdPtBi. We also find our experimental results to be consistent and in good agreement with theoretical predictions. Therefore, our study demonstrates the topological electronic state of half-Heusler GdPtBi crystals and also describes the shape of the anisotropic Fermi-surface experimentally.

Acknowledgements

This work was financially supported by the King Abdullah University of Science and Technology (KAUST) Office of Sponsored Research (OSR), Saudi Arabia, under Award No. CRF-2015-2549-CRG4, and the China Postdoctoral Science Foundation No. Y6BK011M51. W.H.W acknowledges support from the National Natural Science Foundation of China (No.11974406) and Fujian Innovation Academy, Chinese Academy of Sciences.

Conflicts of interest

There are no conflicts to declare.

Supplementary Material

See Supplementary Material for the elaborate experimental details, hysteresis loops, angular dependence of LMR and Intrinsic PHE curves.

References

[1]S. Chadov, X. Qi, J. Kubler, G. H. Fecher, C. Felser, and S. C. Zhang 2010 *Nat. Mater.* **9,** 541.

[2]H. Lin, L. A. Wray, Y. Xia, S. Xu, S. Jia, R. J. Cava, A. Bansil, and M. Z. Hasan 2010 *Nat. Mater.* **9,** 546.

[3]Z. Hou, W. Wang, G. Xu, X. Zhang, Z. Wei, S. Shen, E. Liu, Y. Yao, Y. Chai, Y. Sun, X. Xi, W. Wang, Z. Liu, G. Wu, and X.-x. Zhang 2015 *Phys. Rev. B* **92,** 235134.

[4]H. Zhu, J. Mao, Y. Li, J. Sun, Y. Wang, Q. Zhu, G. Li, Q. Song, J. Zhou, Y. Fu, R. He, T. Tong, Z. Liu, W. Ren, L. You, Z. Wang, J. Luo, A. Sotnikov, J. Bao, K. Nielsch, G. Chen, D. J. Singh, and Z. Ren 2019 *Nat. Commun.* **10,** 270.

[5]S. Bhattacharya, A. L. Pope, R. T. Littleton, T. M. Tritt, V. Ponnambalam, Y. Xia, and S. J. Poon 2000 *Appl. Phys. Lett.* **77,** 2476.

[6]O. Pavlosiuk, D. Kaczorowski, and P. Wisniewski 2016 *Phys. Rev. B* **94,** 035130.

[7]J. Zhang, Z. Hou, C. Zhang, J. Chen, P. Li, Y. Wen, Q. Zhang, W. Wang, and X. Zhang 2019 *Appl. Phys. Lett.* **115,** 172407.

[8]M. Hirschberger, S. Kushwaha, Z. Wang, Q. Gibson, S. Liang, C. A. Belvin, B. A. Bernevig, R. J. Cava, and N. P. Ong 2016 *Nat. Mater.* **15,** 1161.

[9]H. J. Kim, K. S. Kim, J. F. Wang, M. Sasaki, N. Satoh, A. Ohnishi, M. Kitaura, M. Yang, and L. Li 2013 *Phys. Rev. Lett.* **111,** 246603.

[10]L. X. Yang, Z. K. Liu, Y. Sun, H. Peng, H. F. Yang, T. Zhang, B. Zhou, Y. Zhang, Y. F. Guo, M. Rahn, D. Prabhakaran, Z. Hussain, S. K. Mo, C. Felser, B. Yan, and Y. L. Chen 2015 *Nat. Phys.* **11,** 728.

[11]T. Liang, J. Lin, Q. Gibson, T. Gao, M. Hirschberger, M. Liu, R. J. Cava, and N. P. Ong 2017 *Phys. Rev. Lett.* **118,** 136601.

[12]H. Li, H. He, H.-Z. Lu, H. Zhang, H. Liu, R. Ma, Z. Fan, S.-Q. Shen, and J. Wang 2016 *Nat. Commun.* **7,** 10301.

[13]S.-M. Huang, S.-Y. Xu, I. Belopolski, C.-C. Lee, G. Chang, B. Wang, N. Alidoust, G. Bian, M. Neupane, C. Zhang, S. Jia, A. Bansil, H. Lin, and M. Z. Hasan 2015 *Nat. Commun.* **6,** 7373.

[14]H. B. Nielsen and M. Ninomiya 1983 *Phys. Lett. B* **130,** 389.

[15]D. T. Son and B. Z. Spivak 2013 *Phys. Rev. B* **88,** 104412.

[16]A. A. Burkov 2017 *Phys. Rev. B* **96,** 041110.

[17]M. Wu, G. Zheng, W. Chu, Y. Liu, W. Gao, H. Zhang, J. Lu, Y. Han, J. Zhou, W. Ning, and M. Tian 2018 *Phys. Rev. B* **98,** 161110.

[18]T. Suzuki, R. Chisnell, A. Devarakonda, Y. T. Liu, W. Feng, D. Xiao, J. W. Lynn, and J. G. Checkelsky 2016 *Nat. Phys.* **12,** 1119.

[19]J. Barthel 2018 *Ultramicroscopy* **193,** 1.

[20]X. Huang, L. Zhao, Y. Long, P. Wang, D. Chen, Z. Yang, H. Liang, M. Xue, H. Weng, Z. Fang, X. Dai, and G. Chen 2015 *Phys. Rev. X* **5,** 031023.

[21]P. Li, Y. Wen, X. He, Q. Zhang, C. Xia, Z.-M. Yu, S. A. Yang, Z. Zhu, H. N. Alshareef, and X.-X. Zhang 2017 *Nat. Commun.* **8,** 2150.

[22]M. F. Hundley, M. Hawley, R. H. Heffner, Q. X. Jia, J. J. Neumeier, J. Tesmer, J. D. Thompson, and X. D. Wu 1995 *Appl. Phys. Lett.* **67,** 860.

[23]L. P. He, X. C. Hong, J. K. Dong, J. Pan, Z. Zhang, J. Zhang, and S. Y. Li 2014 *Phys. Rev. Lett.* **113,** 246402.

[24]G. Xu, Z. Hou, Y. Wang, X. Zhang, H. Zhang, E. Liu, X. Xi, F. Xu, G. Wu, X.-x. Zhang, and W. Wang 2017 *J. Phys: Condens. Mater.* **29,** 195501.

[25]P. Li, C. H. Zhang, J. W. Zhang, Y. Wen, and X. X. Zhang 2018 *Phys. Rev. B* **98,** 121108.

[26]H. X. Tang, R. K. Kawakami, D. D. Awschalom, and M. L. Roukes 2003 *Phys. Rev. Lett.* **90,** 107201.

1